Fuel 289 (2021) 119820

Contents lists available at ScienceDirect

Fuel

journal homepage: www.elsevier.com/locate/fuel

Full Length Article

Detection of weakly bound clusters in incipiently sooting flames via ion seeded dilution and collision charging for (APi-TOF) mass spectrometry analysis

Francesco Carbone [a,b,*], Manjula R. Canagaratna [c], Andrew T. Lambe [c], John T. Jayne [c], Douglas R. Worsnop [c], Alessandro Gomez [b,*]

[a] Department of Mechanical Engineering, University of Connecticut, 191 Auditorium Road, Unit 3139, Storrs, CT 06269-3139, USA
[b] Department of Mechanical Engineering and Materials Science, Yale University, 9 Hillhouse Avenue, New Haven, CT 06520-8286, USA
[c] Aerodyne Research Inc., 45 Manning Road, Billerica, MA 01821-3976, USA

ARTICLE INFO

Keywords:
Soot inception
Collision charging
Chemical ionization
Mass spectrometry
Flame sampling

ABSTRACT

This study introduces an atmospheric pressure chemical ionization method that relies on low-energy thermal collisions (i.e., <0.05 eV) of aerosolized analytes with bipolar ions pre-seeded in a sample dilution flow and allows for the detection of weakly bound molecular clusters. Herein, the potential of the method is explored in the context of soot inception by performing mass spectrometric analysis of a laminar premixed flame of ethylene and air whose products are sampled through a tiny orifice and quickly diluted in nitrogen pre-flowed through a Kr_{85} based neutralizer to generate the bipolar ions. Analyses were performed with an Atmospheric Pressure Interface Time-of-Flight (APi-TOF, Tofwerk AG) Mass Spectrometer whose high sensitivity, mass accuracy, and resolution (over 4000) allowed for the discrimination of the flame products from the pre-seeded ions. Since ionization of neutrals occurs by either ion attachment or charge exchange following ion collision, the identification of the origin of each peak in the measured mass spectra is not-trivial. Nevertheless, the results provide valuable information on the overall elemental composition of the neutral flame products ionized in either polarity. Results show that the clustering of hydrocarbons lighter than 400 Da and having a C/H ratio between 2 and 3 leads to soot inception in the flame. The dehydrogenation of the flame products, expected to occur as they are convected in the flame, is observed only for measurements in positive polarity because of a higher probability of soot nuclei and precursors to get a positive rather than a negative charge.

1. Introduction

Soot formation is a longstanding and, to some extent, unsolved problem of combustion science and technologies, affecting human health [1] and climate change [2] because of the emissions of pollutant carbonaceous particles. Several decades of studies ascertained that soot forms in flames via multiple chemical and physical transformations that progressively convert the parent fuel molecules into larger molecules, molecular clusters, nano-sized particles, and, eventually, their micron-sized aggregates [3–25]. Undoubtedly the formation of the molecular clusters (i.e., the smallest particle nuclei) of the carbonaceous condensed phase, which is referred to as soot inception (or nucleation), is critical in determining the ensuing evolution toward the formation of larger particles. It is also the least understood process involved during such transformations [12,13,16,22–25]. The scientific community broadly agrees about the role played by Polycyclic Aromatic Hydrocarbons (PAHs) in the generation of a carbonaceous condensed phase in flames [3–19]. However, there is not an accepted (and unavoidably arbitrary) threshold value of the size or mass that can be used to distinguish between large molecules that compose the gas phase and small molecular clusters that can be considered as particle nuclei [20,22–25].

The lack of a fundamental understanding of the soot inception process is in great part related to the shortage of experimental approaches to characterize quantitatively and directly the carbonaceous molecular clusters that eventually are converted to mature particles. Traditionally, fundamental soot inception studies were performed in laminar premixed

* Corresponding authors at: Department of Mechanical Engineering, University of Connecticut, 191 Auditorium Road, Unit 3139, Storrs, CT 06269-3139, USA (F. Carbone); Department of Mechanical Engineering and Materials Science, Yale University, 9 Hillhouse Avenue, New Haven, CT 06520-8286, USA (A. Gomez).
E-mail addresses: carbone@uconn.edu (F. Carbone), alessandro.gomez@yale.edu (A. Gomez).

https://doi.org/10.1016/j.fuel.2020.119820
Received 5 October 2020; Received in revised form 16 November 2020; Accepted 18 November 2020

flames [e.g.,3,5,7,8,10,12–15,20], in many instances at low pressures to implement molecular beam sampling [26] followed by mass spectrometric analyses of the gas molecules [e.g.,3,5,7] or ions and naturally charged particles [e.g.,7,27]. In the cited pioneering flame studies of the '80 s, low resolution mass spectrometric techniques were used to detect neutral gas molecules via aggressive electron impaction ionization (i.e., with standard electron energy being 70 eV) while the use of comparatively less destructive photoionization approaches was limited to the off-line analysis of the components desorbed and ionized by a laser from thermophoretically sampled flame soot samples [28]. More recently, the development of tunable photoionization approaches, eventually implemented with the use of VUV synchrotron light sources, enabled the ionization of a large variety of molecules with the ability to discriminate among isomers [e.g.,29–31] and the online detection of a progressively broader range of particle constituents via aerosol mass spectrometry approaches [e.g.,32–37]. At the same time, the continuous improvement in the resolution of the used mass spectrometers and orbitraps enhanced the level of details about the composition of the molecular constituents of soot even using the traditional Laser Desorption Ionization techniques [e.g.,21,23,38,39]. Despite all the advances, even the most gentle photoionization approaches break apart weakly-bond molecular clusters [36,37,40] that form in the flame at temperatures of the order of 2000 K. Indeed each photon in the nearly-visible spectral interval that is able to induce ionization has energy higher than 1 eV, which is nearly equivalent to the average kinetic energy of a molecule (or ion) at temperatures of 7700 K. It appears that existing experimental data about the mass spectra of flame products necessarily have a gap in the mass interval of relevance to the transition from molecules to particles that the community should attempt to fill.

In addition to the limitations imposed by the used diagnostic techniques, the lack of quantitative information about soot inception is amplified by the paucity of studies that provide concurrently, in the same flame, measurements of both the gas molecule population, including some PAHs, and the soot particles [14,15,24]. Characterizations of the first type usually do not include measurements of PAHs composed of more than two rings (i.e., naphthalene) [14,29–31] and only in rare cases provide quantitative measures of heavier species with molecular weight up to approximately 300 Dalton (Da) [24]. On the other hand, analysis of the smallest detectable soot particles is limited either to the characterization of their molecular components [20,21,23] or to the quantitation of already formed particles with sizes larger than 2 nm that are approximately heavier than 3000 Dalton, if assumed spherical and with a mass density of 1.2 g/cm^3 [12]. It appears that the bulk of scientific literature misses information in the mass (size) range between 150–300 Da (~0.8–1 nm) and 3000 Da (~2 nm) that can be only partially filled by performing High-Resolution Differential Mobility Analyses (HR-DMA) of samples extracted from the flame via dilution sampling [15]. Unfortunately, the best DMAs on the market lack the necessary resolution to complement the dimensional analysis with a chemical characterization of the "particles".

This work aims at introducing an extremely gentle chemical ionization scheme (energy lower than 0.05 eV) to obtain much needed mass spectrometric results to track soot inception in the relevant interval of masses where the distinction between molecules, molecular clusters, and particles is dubious. The results are discussed by overlooking the semantic problem of such a distinction [25] because in many instances large molecules (e.g., hemoglobin and other globular proteins) behave as particles in terms of transport properties (e.g., [41]) and optical properties (e.g., with broadband visible absorption/emission [42]). From this perspective, the largest/heaviest materials extracted from the (faintly) luminous zone of an incipiently sooting flame that can be detected by HR-DMA and, in part, by high-resolution microscopy of thermophoretic samples [43], can be considered as "particles" although their size, molecular weight, and composition may suggest that their structures resemble those of large molecules. The ion collision approach used in this study in conjunction with dilution sampling from the flame was recently implemented to enable HR-DMA measurements of particles smaller than 2 nm and/or molecular clusters that are electrically neutral in the flame [43,15]. Exploratory mass spectrometric measurements of these originally neutral clusters are performed in a flame that has been extensively characterized with many diagnostics in terms of both the gas molecules and particles [14,15,43,44], including APi-TOF analyses of the naturally charged flame products [44] and HR-DMA [15,43] of the neutral ones investigated herein.

2. Experimental methods

2.1. Flame of choice and dilution sampling

The investigated laminar ethylene/air premixed flame has a C/O ratio of 0.69 and an unburnt gas velocity of 58.7 mm/s. In this study, the flame is stabilized on a stainless-steel honeycomb burner (nozzle OD 48 mm) equipped with a plate located 40 mm above the nozzle and an annulus (OD 76 mm) through which nitrogen flows at 0.21 m/s to shield the flame from the surroundings and minimize buoyant acceleration as well as flame flickering. This burner configuration has been characterized by a broad variety of experimental techniques [14,15,43,44]. The investigated flame is equivalent [14] also to the one stabilized on different burners, listed as a target in the dataset of the International Sooting Flame Workshop [16].

The analytes are extracted from the zone of the flame where soot inception occurs and a faint broadband orange luminosity appears, at Heights Above the Burner (HABs) between 2.5 mm and 10 mm in 2.5 mm-step increments [15,43,44], thorough an orifice facing the center of the burner nozzle. The orifice is drilled on the (0.127 mm thick) wall of a horizontal stainless-steel tube (OD 6.35 mm) through which 30slpm of nitrogen flow steadily to dilute the sample rapidly. The outlet of the sampling orifice inside the horizontal tube is kept under a small (~600 Pa) and constant under-pressure to allow for the sampling of the flame products, with the approach detailed in [43,15] that is revised compared to the one introduced in [45,46]. Orifice diameters of decreasing sizes from 0.25 mm to 0.08 mm are used to span values of the Dilution Ratio (DR) from 660 to 6400, without changing the value of the applied underpressure and the dilution flow rate. These are equivalent to values of the Dilution to sample Standard flowrate Ratio ($DSR = T_{sample}/T_{flame} \cdot DR$) ranging from 120 to 1150, once one accounts for the increase in the gas density as the temperature of the analytes decreases from that in the flame ($T_{flame} \approx 1680$ K) to the one of the diluted sample ($T_{sample} \approx 300$ K). The approach of keeping the sampling underpressure and dilution nitrogen flowrate constant isolates the effect of dilution on the results because it keeps approximately constant the sampling velocity and, consequently, the perturbation induced by the probe on the flame flow field [15], as well as the time, Δt, for the sample to travel from the flame to the inlet port of the analysis device [43].

2.2. Ion pre-seeded dilution for collision charging and atmospheric pressure interface time-of-flight (APi-TOF) mass spectrometric analysis

Measurements were performed with the Atmospheric Pressure interface (APi) Time-Of-Flight (-TOF) mass spectrometer (APi–TOF, Tofwerk AG) described in [47]. The APi is directly connected to the sampling tube downstream of the flame sampling orifice in a modified configuration compared to the one used to analyze the naturally charged products of the flame [44]. Most of the diluted sample flow is exhausted from the APi through a backpressure regulating valve followed by a vacuum pump, while a small sample flowrate, S_{APi}=0.8slpm, is drawn thorogh a 0.3 mm hole inlet into an atmospheric pressure interface that guides sampled ions into a bipolar TOF mass spectrometer for high-resolution mass spectrometric analysis [47]. The ions are introduced in the dilution flow with a Kr_{85} radioactive charger/neutralizer (model 3077, TSI Inc.) connected to the sampling tube upstream of the sampling orifice, as schematically depicted in Fig. 1. The dilution nitrogen flows

through the neutralizer right before being admitted in the sampling tube so that a variety of ions are generated [48,49] because of collisions of the radioactive decay products (i.e. beta particles and gamma-ray from Kr_{85} decay) with the molecules composing the dilution nitrogen (gas purity greater than 99.9%) and its unavoidable trace impurities. This ion pre-seeding approach was introduced in HR-DMA studies and enables the detection of neutral materials smaller than 2 nm generated by the flame that would otherwise disappear via self-collisions when using traditional diffusion charging methods [15,43]. This is the case because the approach takes advantage of the unavoidably finite time interval, Δt, for the sample to be transported by the flow from the flame sampling orifice to the analysis point, to charge originally neutral materials via collisions with the pre-seeded ions. As a result, the Δt and, with it, the number of self-collisions of the smallest flame-sampled materials that would cause their rapid growth and consequent disappearance, can be minimized.

In this study, the time to dilute and transport the flame sample to the analytic device is kept at a minimum of $\Delta t \sim 30$ ms so that the ratio DR/Δt, controlling the quenching of the sample via self-collisions [43], is raised to values up $\sim 210\ ms^{-1}$, well beyond the range achieved in any previous effort to minimize modifications of the materials extracted from the flame in their path to the analyser [15,43].

The ion pre-seeding also allowed the implementation of the ionization method that is necessary to detect electrical neutral analytes in a non-destructive manner. Since the colliding ions are in thermal equilibrium with the molecules of the cold dilution nitrogen (i.e, temperature < 320 K), their average kinetic energy is smaller than 0.05 eV which is much smaller than the bonding energy of physical clusters of PAHs [40]. The charging of the neutral analytes (i.e., neutral molecules, radicals, molecular clusters, or "particles") follows ion-collisions via either the direct attachment with a physical or chemical bond of the entire ion or one of its charged fragments (ion exchange reaction), including a single proton, or the transfer of an elementary charge via the exchange of an electron. All these mechanisms minimize the potential break-up of weakly bound molecular clusters but, as a significant drawback, ion attachment and ion exchange reactions perturb the composition of the analytes. Additionally, the displacement of part of the analyte (e.g., one of the units composing the cluster) can occur because of the attachment of the colliding charge/ion. This mechanism would fall in the category of the cluster dissociation events that the ion collision approach is trying to minimize but that cannot be avoided totally. While in principle the charging reactions and their induced composition perturbation can be tracked by HR-mass spectrometric analyses of both the pre-seeded ions and the collisionally charged analytes, such comprehensive tracking would be quite convoluted and is beyond the scope of this exploratory study. An additional complication in the quantitative interpretation of the results is related to the estimate of the ionization efficiency which is nontrivial and can be performed possibly only as an average for lumped families of peaks in the mass spectra (e.g., all peaks of species with similar values of the electrical mobility/sizes) with the approach introduced in [50] and used preliminarily in [15,43]. These complications are the price to pay for enabling the detection of weakly bond clusters and will be the object of future studies in which ion seeding in the dilution flow will be implemented in different ways (e.g., using different ion generation devices and/or compositions of the dilution gas) to change the composition and number of ions pre-seeded in the dilution flow. This study focuses on the overall trends in the elemental composition of the gently ionized flame products without tracking the origin of any single peak composing the measured mass spectra.

High mass resolution and accuracy of the measurements are needed for the chemical characterization of the analytes. The diluted flame products certainly contain carbon, hydrogen, oxygen, and nitrogen (C, H, O, and N) and the identification of the peaks in the mass spectra is possible because the atomic weights of elements differ from their nominal integer values by a fractional *mass defect* that is element-specific [44,47,51]: C has zero mass defect (nominal monoisotopic mass of 12 Da); H and N have positive mass defects of 0.007825 and 0.003074 (nominal monoisotopic masses of 1 Da and 14 Da), respectively; O has a negative mass defect of 0.005085 (nominal monoisotopic mass of 16 Da). The APi-TOF [47] used in this work is configured to analyze the interval of mass over charge, m/z, below 3000 Thomson, *Th*, equivalent to 3000 Dalton, Da, for analytes with unit elementary charge, with a resolution, $m/\Delta m$, above 4000. The instrument is mass calibrated for measurements in both charge polarities in an m/z range between 100Th and 1500Th with an accuracy better than 0.001%. Mass calibrations are performed in both polarities by electrospraying several mass standards [44]. The standards include ammonium phosphate, sodium dodecyl sulfate, sodium taurocholate, reserpine, a few tetra-alkyl ammonium halides [52], and the Ultramark 1621 mixture [53] which have all been previously utilized to perform the mass calibration of the Tofwerk TOFs to higher m/z ranges [54].

Since the concentration of the analyzed materials decreases substantially with increasing m/z, we have converted the measured mass spectrum from ion count rates, d(I)/dt, versus m/z to a more compact graphical representation of the results. In this representation, the mass spectrum is shown as $\frac{d(N_e)}{d[ln(m/z)]}$ versus m/z, as described previously [44]; the volumetric number concentration, $N_e = DSR \cdot \frac{I}{\eta_{APi} \cdot S_{APi}}$, is inferred by dividing the electric current measured by the Mass Spectrometer for a given m/z by the APi flowrate, S_{APi}, and the value of the APi transmission efficiency, η_{APi}, (which is estimated at ≈0.2% [44,47]) and multiplying it by the Dilution to sample Standard flowrates Ratio (DSR) to rescale the number to in-flame conditions. The results are processed by assuming $\eta_{charg} = 1$, that is, without considering any correction to account for a non-unitary ionization efficiency, η_{charg}, of the collision charging method. This effect is not accounted for since it is difficult to estimate with a species and polarity-dependence that is not a smooth function of m/z, and since any given neutral compound can generate multiple ion peaks by undergoing different charge exchange mechanisms. The value of η_{charg} is not expected to exceed its steady-state limit that results from many collisions of the analytes with a large number of ions. The limiting steady-state value is substantially smaller than 10^{-2} for the analyzed flame products that have mobility diameters (molecular weights)

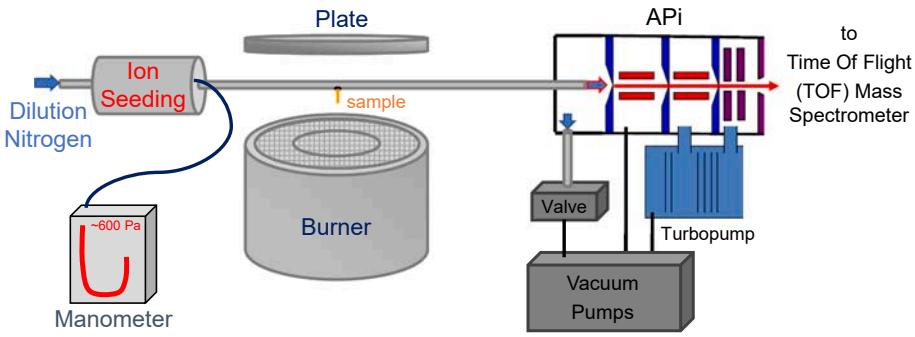

Fig. 1. Experimental configuration to extract, dilute, and collision-charge the flame products, enabling APi-TOF analyses of originally neutral molecular clusters.

smaller than 2 nm (i.e, <2000 Da). Additionally, the time Δt available for collisions to occur is much shorter than the time to achieve the limiting steady-state condition [43,50]. As a result, the number concentration of neutrals that yields the measured peaks in the mass spectra are expected to be more than three orders of magnitude larger than the N_e reported for the analytes effectively charged via collisions [43]. A more accurate estimate of the value of the ionization efficiency for the measured materials also requires additional dedicated studies that are beyond the scope of this study.

3. Results and discussion

3.1. Mass spectra of the pre-seeded ions with and without sampled flame products

Fig. 2 shows the mass spectra of cations (top panel) and anions (bottom panel) pre-seeded in the dilution nitrogen, that is, without any flame sample, superimposed to those of the flame products that are charged upon mixing with such pre-seeded ions, after being sampled from the flame at HAB = 2.5 mm with the 0.25 mm orifice, diluted in nitrogen with a Dilution Ratio DR = 660, and transported to the APi-TOF inlet during a time interval Δt (DR/Δt ≈ 22 ms^{-1}). The insets in the figure show enlarged views of the *m/z* abscissa with linear ordinate to highlight some differences in the nominal masses where high peaks are positioned. Although the pre-seeded ions do not undergo dilution, all results are corrected for the dilution factor applied to the flame sample for data processing consistency and to allow for a direct quantitative comparison of the signals associated with the two different classes of analytes [43]. The measured mass spectra are composed of individual, well resolved, but densely packed peaks, some of which are positioned at the same nominal value of *m/z*. In many instances, the measured mass spectra have sufficiently high resolution to allow for the nontrivial distinction of the peaks associated with either the pre-seeded ions or the collision-charged flame products. However, such a distinction cannot be visualized easily in the classical representation of Fig. 2 and is most challenging for the samples extracted at HABs below 5 mm where the flame does not emit any yellow spontaneous luminosity associated with the presence of soot particles (see inset in Fig. 2 showing an image of the flame and an arrow pointing to the sampling position). In this region, most of the flame products do not grow past values of masses (*m/z*) greater than 300 Da (Th), typical of the largest PAHs that can be detected and quantified in flames [14,24,29–31] as well as of the ions seeded in the dilution flow with the Kr_{85} source.

Fig. 3 is the counterpart of Fig. 2 at HAB = 10 mm that is the highest sampling position considered in this work, well within the luminous zone of the flame caused by the spontaneous thermal emissions of soot particles (see flame image inset). Although a direct comparison of HR-DMA and APi-TOF measurements is not reported in this manuscript, all the mass spectra reported in this study, including the ones of Figs. 2 and 3, are in qualitative and quantitative agreement with the published results of HR-DMA measurements of the same samples [43], as shown in the case of naturally charged flame products [44]. Additionally, at HAB = 10 mm, the flame generated materials can be imaged via Transmission Electron Microscopy after being sampled via thermophoresis on appropriate substrates, occupy volume fraction of approximately $3 \cdot 10^{-9}$ and have light scattering equivalent average size of about 2 nm (i.e., mass roughly equivalent to 3000 Da) as detailed in [15].

Fig. 3 reveals that the mass spectra of the flame products charged via collisions with the ions pre-seeded in the dilution flow extend to larger values of *m/z*, as the sampling position is shifted downstream in the flame. As a result, the distinction between the signals stemming from flame sampling from those of the pre-seeded ions is greatly facilitated for *m/z* larger than 400 Th. The detection of materials of increasing *m/z* at higher HABs is not surprising because the pyrolysis and molecular growth occurring in the flame are expected to lead to the generation of progressively larger PAHs and eventually to the nucleation of soot particles [e.g.,9,14,15,17,18,24]. On the other hand, the observation that the number concentrations of materials heavier than 400 Da (i.e., bigger than ~ 1 nm) decreases with increasing *m/z* is nontrivial because the number concentration of soot nuclei can be as large as those of small aromatics [15,24]. While the transmission efficiency of the APi-TOF could mildly decrease at larger *m/z* which could contribute to some of the observed reduction in the signal, the observed reduction is much sharper than expected because of this effect and is consistent with the one observed by HR-DMA measurements [15,43]. As a consequence, the results indicate that the largest detected materials are those originating from the first mode of the size distribution of the incipient soot measured by HR-DMA and causing the presence of the yellow luminosity of the flame [15]. One can also observe, in the insets of Fig. 3, that most of the high peaks associated with the gaseous species with a molecular weight lighter than 180 Da disappear from the mass spectra of the collision charged flame samples collected in the sooting zone of the flame. This probably happens because small charged PAHs adsorb/condense on (or simply transfer their charge to) the simultaneously sampled incipient

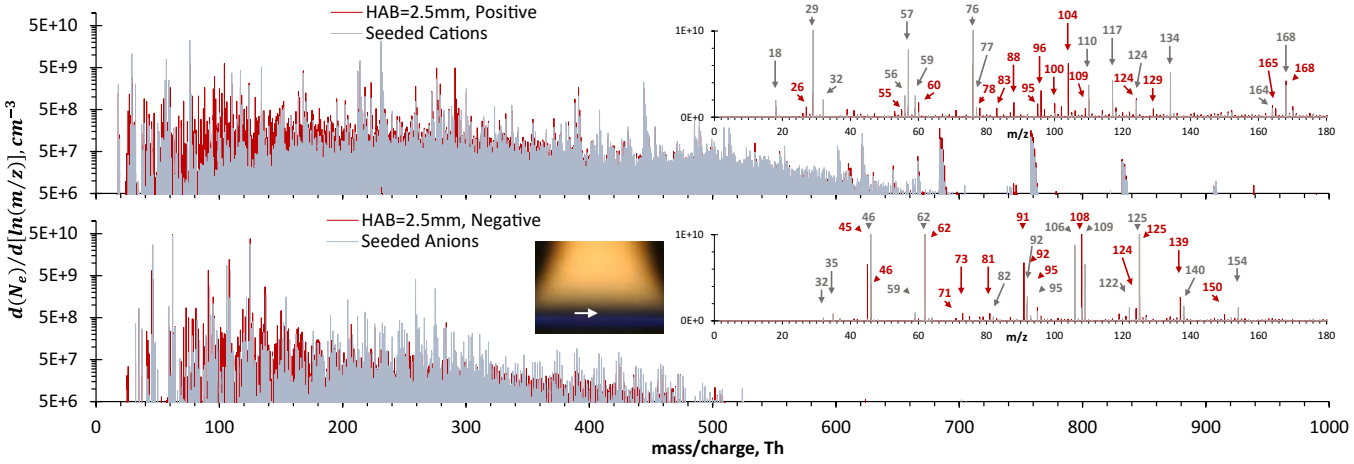

Fig. 2. Mass spectra of cations (top panel) and anions (bottom panel) pre-seeded in the dilution nitrogen (gray peaks) compared to those of the flame products sampled at HAB = 2.5 mm (red peaks), diluted with DR/Δt ≈ 22 ms^{-1}, and charged in the correspondent polarity via collisions with the pre-seeded ions. All number concentrations are corrected for the dilution applied to the flame sample. Spectral insets show enlarged abscissa and linear ordinates to highlight high peaks. Image inset: flame with an arrow pointing at the sampling position. (For interpretation of references to color in this figure legend, the reader is referred to the web version of this article.)

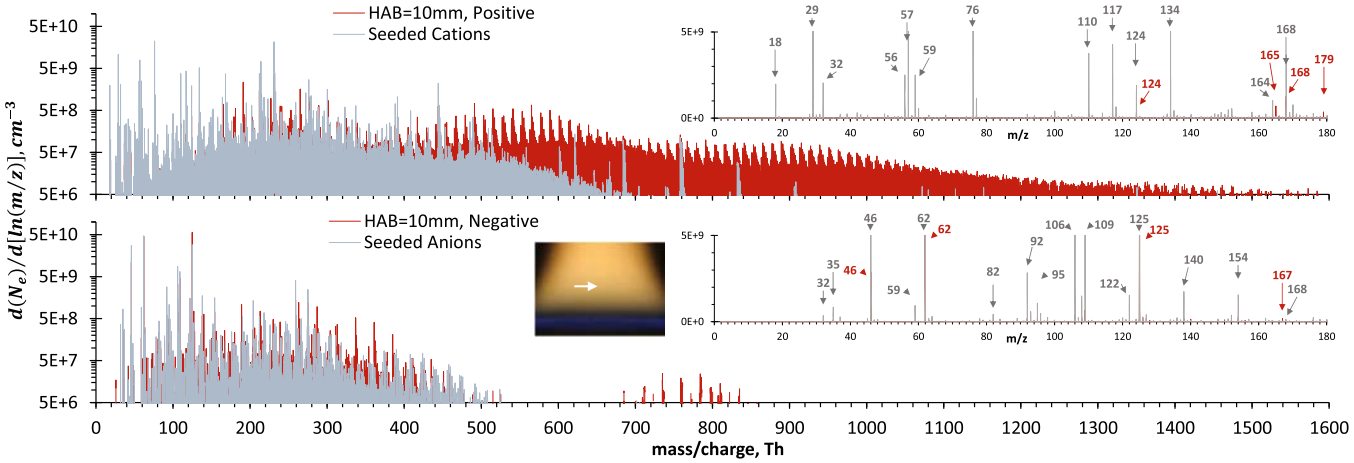

Fig. 3. Mass spectra of the flame products sampled at HAB = 10 mm (red peaks), diluted with DR/Δt ≈ 22 ms^{-1}, and charged in either positive (top panel) or negative (bottom panel) polarity via collisions with the ions pre-seeded in the dilution nitrogen (gray peaks). All number concentrations are corrected for the dilution applied to the flame sample. Spectral insets show enlarged abscissa and linear ordinates to highlight high peaks. Image inset: flame with an arrow pointing at the sampling position. (For interpretation of the references to color in this figure legend, the reader is referred to the web version of this article.)

soot particles, while the flame sample is transported to the APi-TOF inlet in the sampling and charging system. Furthermore, the mass spectrum of the collision charged flame products appear to be multimodal at HAB = 10 mm, with the first mode being superimposed to the only one composing the mass spectra of the pre-seeded ions, that is centered at around 250Th. Two additional modes can be identified at approximately 550Th and 950Th in positive polarity whereas only one additional mode is detected around 750Th in negative polarity. The rough equal-spacing of the modes suggests the occurrence of molecular clustering leading to incipient soot.

Before diving deeper into the analysis of the results, one should calculate the number concentration of the detected materials by integrating their peak(s) to perform a meaningful quantitative interpretation of the results in Figs. 2 and 3. The calculation entails integrating the mass spectra and the results are determined not only by the peak widths and maxima but also by their packing density (i.e., number of peaks per *m/z* interval). The resulting dilution corrected number concentrations of ions and collision charged materials that reach the APi inlet with either a positive or negative charge after surviving recombination and diffusion losses in the sampling system are 7.6 ± 0.8·$10^7$$cm^{-3}$ and 4.9 ± 0.5·$10^7$$cm^{-3}$, respectively. The reported standard deviation reflects the variation across measurements without flame sampling (pre-seeded ions) and for all the flame samples extracted at different HABs. The values are different in opposite polarities because of undetectable electrons and because of the size dependence of diffusion losses [43], but are in excellent agreement with those reported in published HR-DMA measurements performed with the same ion pre-seeding and collision charging approach [43]. The agreement confirms the potential of the implemented technique to provide (semi)quantitative results for the development of methods to estimate the ionization efficiency of the detected materials [e.g.,15]. Most importantly, regardless of the applied dilution and sampling HAB, the number concentrations are not affected by the naturally charged materials generated by the flame because the diluted flame chemi-ions, simultaneously sampled from the flame [44], are at least one order of magnitude less abundant in terms of number concentration compared to those shown in Figs. 2 and 3. As a consequence, the peaks in Figs. 2 and 3 can be associated either with the pre-seeded ions or with flame products that were originally neutral in the flame but acquired a charge upon mixing and colliding with the pre-seeded ions.

A close inspection of some easily identifiable high peaks in Figs. 2 and 3 reveals that the pre-seeded ions generated by exposing dilution nitrogen (and its unavoidable impurities) to the Kr_{85} source include NH_3H^+, N_2H^+ and N_4H^+ (at 18Th, 29Th, and 57Th in the top panels) and NO_2^- and NO_3^- (at 46Th and 62Th in the bottom panels). These ions are among the many causing charging of the flame samples in the used chemical ionization scheme and are representative of the overall composition of the pre-seeded ions, as clarified in the ensuing discussion. A closer examination of the insets of Figs. 2 and 3 reveals in all the measured mass spectra that the high peaks are *not* distributed preferentially at odd (e.g., ionized radicals and/or protonated/deprotonated species [17,44]) or even (e.g., ionized stable hydrocarbons) values of *m/z* and there is no apparent correlation between the position of the peaks detected in opposite polarities. The nonsystematic positioning of these high peaks is in direct contrast with the prevalence of odd *m/z* peaks shifted of 2Th for results in opposite polarities observed in the measurements of naturally charged flame products which suggested protonation and deprotonation as prevalent natural charging mechanisms caused by the flame chemi-ions [44]. On the other hand, one can notice a close relationship in both panels of Fig. 2 (and partially of Fig. 3) between the spectra of the pre-seeded ions and those of the flame products that acquire a charge in the same polarity because of collisions with such ions. The collision charged flame samples yield several peaks shifted by + 1Th in positive polarity (e.g., at *m/z* = 60, 78, and 165 Th) and by −1Th in negative polarity (e.g., at *m/z* = 45, 91, 108, and 124 Th), as compared to those of the pre-seeded cations (e.g., at *m/z* = 59, 77, and 164 Th) and anions (e.g., at *m/z* = *m/z* = 46, 92, 109, and 124 Th). This relationship suggests that the pre-seeded ions can undergo hydrogenation or dehydrogenation upon colliding with the sampled flame products. It appears that (both charged and neutral) flame products are prone to exchange one of their hydrogen atoms (with or without the paired electron) upon colliding with an ion of any type either at high temperature in the flame or low temperature in the sampling, dilution, and charging system. In the mass spectra of the flame products, one can also notice the appearance of completely different peaks compared to those of the pre-seeded ions. These “flame” peaks result from the ionization of neutral flame products such as those distinguishable in Fig. 2 at 95Th (e.g., $C_4H_5N_3^+$ and $C_6H_9N^+$), 96Th (e.g., $C_4H_6N_3^+$) and 104Th (e.g., $C_8H_8^+$) in positive polarity and at 71Th (a mix of $C_3H_3O_2^-$ and $C_2H_3N_2O^-$), 73Th (including $CHN_2O_2^-$ and $C_2H_3NO_2^-$) and at 150Th (including $C_2H_2N_2O_6^-$ and $C_2H_4N_3O_5^-$) in negative polarity. It appears that nitrogen, and, at least in negative polarity, oxygen must be considered in addition to hydrogen and carbon, if one wants to interpret the measured mass spectra in terms of the elemental composition of the detected materials. The peak-to-peak analysis at larger *m/z* is beyond the scope of this study and becomes unachievable at sufficiently large

values of m/z with any instrumental resolution. Indeed, the number of possible combinations of elements that result in extremely close values of m/z increases exponentially with m/z itself.

3.2. Mass defect plots: Distinguishing the collision charged flame products from the pre-seeded ions

Mass defect plots offer an effective method for tracking the chemical composition even without assigning the elemental composition of each peak in a complex mass spectrum. In a mass defect plot, the mass defect of each peak in the mass spectrum is plotted against its nominal integer value of m/z [44,51], as in Fig. 4. In such plots, families of compounds with the same chemical backbone but differing from each other by the addition or subtraction of the same subunit (e.g., hydrocarbons with different numbers of C_CH_H units) show up on straight lines because their mass defect is proportional to their mass. The slope of the line is a function of the elemental composition of the subunit (i.e., $C_CH_HO_ON_N$), which affects the mass defect, and the number of elementary charges, which affects the m/z. In general, the mass defect at a given m/z of multiply charged materials is significantly larger than the one of their singly charged counterparts. Fortunately, the kinetic theory of gases predicts that the generation of multiply charged materials via collision charging is extremely unlikely in the sub-3000 Da (sub-2 nm) mass (dimensional) range [50,55]. As a consequence, potential complications in the interpretation of the mass defect plots related to multiple charges can be safely neglected in most of the cases in this study.

The mass defect plots were used in our previous study to infer trends in the global elemental composition of naturally charged hydrocarbons sampled from the flame [44] by taking advantage of the fact that the slope of the line followed by singly charged (i.e., $|z|=1$) materials with the same elemental composition ratios increases for hydrocarbons with increasing hydrogen content ($6.0\cdot10^{-4}$Th^{-1} for C/H = 1) and decreases to negative values for oxygenated carbon with increasing oxygen content ($-4.1\cdot10^{-5}$Th^{-1} for C/O = 3) [44,51].

In this study, the interpretation of the results is further complicated by the presence of nitrogenated compounds that are certainly present in the pre-seeded ions. Additionally, there is a need to introduce an approximate methodology (taking advantage of the high resolution of the measurements) to distinguish in the mass spectra the peaks associated with the flame products charged via collisions with the pre-seeded ions from the ones associated with the pre-seeded ions themselves. This methodology can rely on the use of the mass defect plots because one would expect that the flame products have elemental compositions different from that of the ions generated by radioactive ionization of relatively pure nitrogen.

The top panels of Fig. 4 show the mass defect plots of the cations (top left panel) and anions (top right panel) pre-seeded in the dilution system. They are compared in the corresponding middle panels to those of charged materials stemming from their collisions with flame products sampled at HAB = 5 mm with the 0.25 mm orifice (DR/Δt $\approx$ 22 ms^{-1}). The correspondent plots in either polarity are superimposed on each other in the bottom panels of Fig. 4. Fig. 4 depicts also the straight lines of increasing slope characterizing the trends followed by singly charged oxidized carbon with C/O = 3, hydrocarbons (with C/H = 3,2, and 1), and hydrazine clusters (H/N = 2), the latter having the largest slope ($11.7\cdot10^{-4}$Th^{-1}). The lines do not identify the actual composition of each peak composing the mass spectra uniquely because they do not account for materials containing more than 2 elements (e.g., oxygenated hydrocarbons have smaller mass defects compared to a pure hydrocarbon with the same molecular weight and C/H ratio). Nonetheless, the lines enable a visual inspection of the results that highlight differences in the elemental compositions.

In Fig. 4 the peaks of the pre-seeded cations mostly appear between the characteristic lines for H/N = 2 and C/H = 1, whereas those of anions are slightly shifted toward smaller mass defects, with a secondary branch positioned at highly negative values of mass defects that is attributable to multiply charged oxygenated ions generated by exposing the dilution nitrogen to Kr_{85} decay. The mass defect plots qualitatively confirm the previous observations that the pre-seeded ions contain nitrogen and that a substantially larger fraction of measured anions contain oxygen compared to cations. More importantly, the inspection of the mass defect plots in the middle and bottom panels of Fig. 4, evidence the subtle differences in the position of the peaks measured during flame sampling compared to those of the pre-seeded ions alone, even at the same nominal value of m/z. Such differences were already mentioned, although they could not be readily visualized, when discussing Figs. 2 and 3 but become apparent in the bottom panel of Fig. 4 because the number concentration of the collision charged flame products peaks at a different value of the mass defect as compared to the pre-seeded ions of the same polarity.

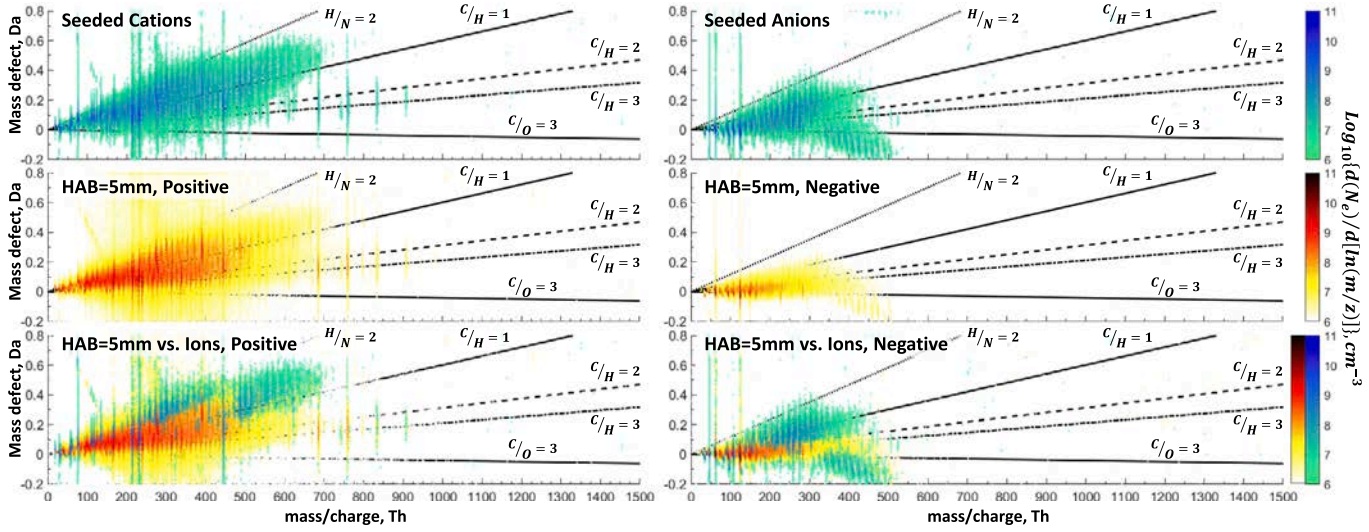

Fig. 4. Mass defect plots of cations (top left panel) and anions (top right panel) pre-seeded in the dilution nitrogen compared to those of the flame products (middle panels) that were sampled at HAB = 5 mm, diluted with DR/Δt $\approx$ 22 ms^{-1} and charged via collisions with the pre-seed ions. All number concentrations are corrected for the dilution applied to the flame sample and shown in colors based on the color-bars on the right. Plots of either polarity are superimposed in the bottom panels to visualize where the concentration of the flame samples exceeds that of the pre-seeded ions. The characteristic lines depict the mass defects of singly charged oxygenated carbon with C/O = 3, hydrocarbons (with C/H equal to 1, 2, and 3), and hydrazine clusters (H/N = 2).

Fig. 4 demonstrates that it is possible to distinguish the collision charged flame products from the pre-seeded ions mixed with them to trigger their ionization. The distinction is possible even for the flame products sampled at HAB = 5 mm, where it is most challenging because the mass spectra of the pre-seeded ions and collision charged flame products lie in the same range of the m/z and mass defect ranges. This is not surprising since flame products are mostly hydrocarbons whose collision charging generates compounds with much more carbon and less nitrogen (and oxygen) content by comparison with the ions produced by exposing the dilution nitrogen (and its impurities) to the Kr_{85} radioactive decay. The separation of the peaks associated with the flame samples from that of the pre-seeded ions in the mass defect plots is possible thanks to the high resolution of the measured mass spectra and can be implemented with an approximate approach. The approach is based on the subtraction of the "background" mass spectrum of the pre-seeded ions from that of the flame samples of correspondent polarity before plotting the mass defect plots of the collision charged flame products, to remove the peaks associated with the pre-seeded ions that outlast the collisions with the flame samples and reach the APi-TOF inlet. The subtraction removes all the peaks where the number concentration of the pre-seeded ions exceeds those of the collision charged flame samples. In general, such subtraction is not rigorous because the pre-seeded ions are progressively depleted as they transfer their charge via collisions to the analyte [15,50]. Additionally, some spurious peaks may survive the subtraction because some ions may change composition as they collide with the flame samples as discussed for Figs. 2 and 3 (e.g., when they undergo either hydrogenation or dehydrogenation). On the other hand, the subtraction is an acceptable approach to "clean up" the data (e.g., it effectively removes the peaks with large negative mass defects associated with the multiply charged oxygenated anions) and allows one to track visually the overall composition of the collision charged flame products sampled at different HABs and subject to different dilution levels without having to keep track of and discuss the immanent background signal associated to the pre-seeded ions.

3.3. Elemental composition of the flame-generated molecular clusters: "flame aging" and dilution effects

The inclusion of characteristic lines in the mass defect plots not only brings to the fore different classes of compounds in the mass range of interests but also allows us to recognize, via a simple visual inspection, qualitative trends regarding changes occurring in the overall elemental composition of the detected materials when comparing results of different measurements. For example, hydrogenation of the analyte (and/or addition of nitrogen to its carbon backbone) would cause the mass spectra to shift progressively toward characteristic lines with an increasing slope, whereas oxygenation would cause the progressive shift toward characteristic lines of reduced (or more negative) slopes.

To investigate the occurrence of compositional changes as flame-generated hydrocarbon species undergo the pyrolysis/growth leading to soot inception while they are convected downstream of the blue flame front, Fig. 5 shows the dilution-corrected mass spectra of the collision charged flame samples extracted at different HABs with the 0.25 mm orifice, including the results discussed in Figs. 2–4. All mass spectra in Fig. 5 were cleaned of the signal due to the residual pre-seeded ions with the approximate subtraction approach described in the discussion of Fig. 4. The mass defect plots are sorted from top to bottom for the samples extracted at increasing HABs, with the left and right panels used for the measurements in either positive or negative polarity, respectively.

Fig. 5 includes also the five compositional lines introduced in Fig. 4, that are typical of compounds of fixed elemental composition ratios; namely, oxidized carbon with C/O = 3, hydrocarbons (with C/H = 3,2, and 1), and hydrazine clusters (H/N = 2).

At HAB = 2.5 mm, where the flame yellow luminosity caused by soot is not present, the spectra roughly extend to m/z up to 400Th and one can observe the largest differences for measurements in opposite polarities. The fact that many peaks detected in positive polarity are positioned above the line of hydrocarbons with C/H = 1 conforms to the expectation that most of the early formed flame products have large

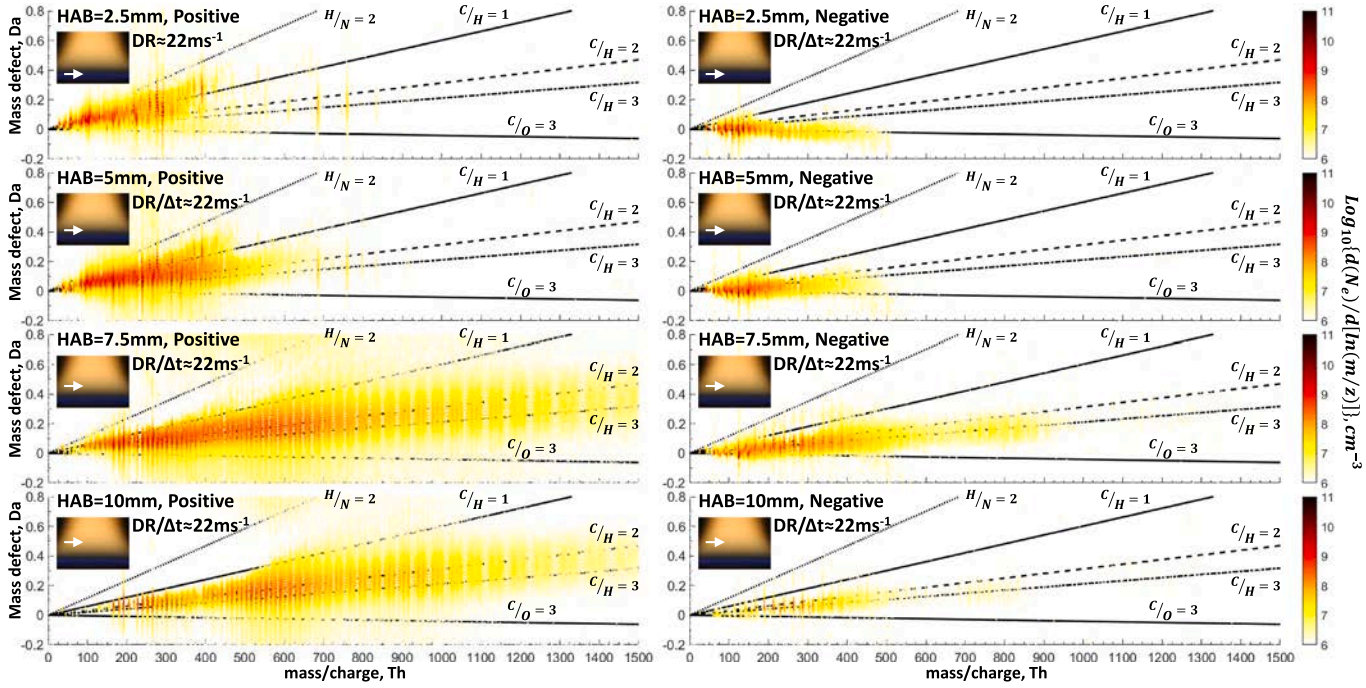

Fig. 5. Mass defect plots of the flame products sampled at HABs from 2.5 mm (top) to 10 mm (bottom), in 2.5 mm increment, diluted with DR/Δt ≈ 22 ms^{-1}, and charged in positive (left panels) and negative (right panels) polarities via collisions with the pre-seeded ions. All number concentrations are net of the contribution of the pre-seeded ions, corrected for the dilution applied to the flame samples, and shown with color-codes based on color-bars to the right. Insets highlight the sampling orifice position in a picture of the flame.

hydrogen content [14,15] and can get nitrogenated because of the attachment of the nitrogen-containing pre-seeded cations. Conversely, in negative polarity, one can detect oxygenated materials because the many measured peaks lie close to a characteristic line of negative slope typical of oxygen-containing materials. The selective detection of oxygenated compounds in negative polarity is associated with two effects: first, the presence of oxygen increases the ability of a compound to capture an electron and get a negative charge without suffering fragmentation, whereas pure hydrocarbons are prone to lose (rather than acquire) an electron and are, consequently, more easily detected in positive polarity. Additionally, most of the pre-seeded anions are already oxygenated so that the attachment of an anion (or one of its fragments) to hydrocarbons is likely to lead to the detection of peaks typical of oxygenated charged compounds. Downstream in the flame, one can notice not only the growth of the flame products but also a pattern typical of dehydrogenation in positive polarity through a reduction in the slope of the characteristic line followed by the detected species and of apparent deoxygenation in negative polarity through an increase in the slope of the characteristic line. The trends cause a progressive reduction in the compositional asymmetry observable in opposite polarities for HAB >5 mm, once the yellow soot luminosity of the flame is fully visible. In this region, soot particles can be detected by different techniques [14,15]. Interestingly the dehydrogenation and molecular growth behavior that is expected to lead to soot inception as flame products are convected downstream in the flame is only evidenced by the measurements in positive polarity. At HAB = 7.5 mm both mass spectra measured in opposite polarities become multimodal for the first time and their mass defect plots evidence not only that the modes are roughly equispaced, as noticed in Fig. 3, but also that the modes are caused by charged materials with constant elemental composition since most of the peaks line-up with a characteristic line C/H between two and three. Somewhat surprisingly, the trends in Fig. 5 are quite similar to those observed for naturally charged materials [44] and highlight the occurrence of clustering and collision charging of hydrocarbons with a molecular weight lighter than 400 Da. Indeed the presence of nitrogen would only slightly increase the slope of the characteristic composition lines, and this minor adjustment does not affect the C/H ratio of the modes that stem from clustering indicated by the measurements in both polarities. The ability to ionize materials without breaking weak bonds allows us to document the occurrence of clustering for flame products that are originally neutral in the flame. The elemental composition and multimodal trends in the results at HAB = 10 mm are similar to those at

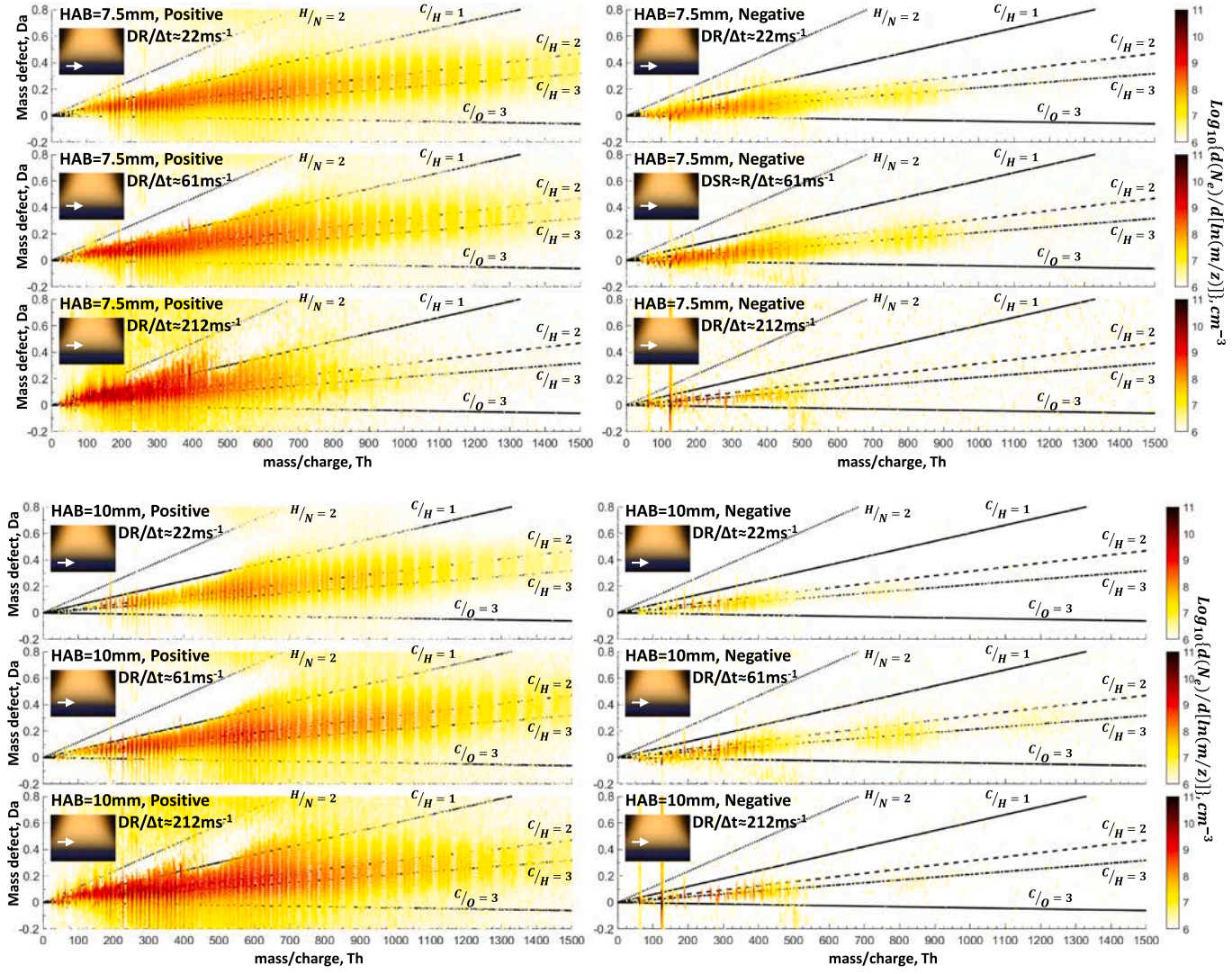

Fig. 6. Mass defect plots of flame products sampled at HAB = 7.5 mm (top panel set) and 10 mm (bottom panel set) that were charged via collisions with the pre-seeded ions after applying different dilutions with DR/Δt ranging from ≈22 ms^{-1} to ≈212 ms^{-1} (top-to-bottom in each set). All number concentrations are net of the contribution of the pre-seeded ions, corrected for the dilution applied to the flame samples, and shown in colors based on color-bars to the right. Measurements were performed in positive (left) and negative (right) polarities.

HAB = 7.5 mm, the biggest difference being the visible reduction in the number concentration measured for compounds lighter than 400 Da in the first mode in both polarities and of all materials in negative polarity. The reduction is related to the ongoing clustering and is so significant that almost no peaks are detected at *m/z* below 200 Th and the second mode is barely visible in negative polarity, as already noticed in the discussion of Fig. 3.

Measurements at increasing dilution levels were performed using sampling orifices of smaller diameters to investigate experimentally if clustering occurs at low temperature in the sampling system rather than at high temperature in the flame. Indeed, the increase of DR/Δt to values (up to ≈212 ms^{-1}) much higher than previously achieved is expected to minimize the sample growth dynamics due to self-collisions in the dilution sampling and charging system and eventually allows to approach conditions of dilution-independent results [43]. Fig. 6 shows the dilution-corrected mass spectra of the collision charged flame samples extracted at HAB = 7.5 mm and HAB = 10 mm with the 0.25 mm (DR/Δt ≈ 22 ms^{-1}), 0.15 mm (DR/Δt ≈ 61 ms^{-1}), and 0.08 mm (DR/Δt ≈ 212 ms^{-1}) orifice, respectively. All mass spectra in Fig. 6 were cleaned of the residual spurious signal originating from the pre-seeded ions as described in the discussion of Fig. 4. The mass defect plots are grouped for the two considered flame sampling positions and sorted for increasingly higher dilutions from top to bottom, with the left and right panels used for the measurements of positive and negative collision charged flame products, respectively. Results at lower HABs are not included in Fig. 6 because they do not show the multimodal behavior that suggests clustering even at the lowest investigated dilution level. Additionally, the compositional trends of the mass defect plots at HAB = 2.5 mm and HAB = 5 mm are virtually identical to those in Fig. 5, regardless of the dilution level, the only minor changes being caused by an increase in the data noise at high dilution related to a relative increase of the spurious contribution of the pre-seeded ions. The increase in noise occurs because the number concentration of the pre-seeded ions in the sampling tube is not affected by dilution as opposed to that of the sampled flame products whose number concentration in the sampling tube changes inversely proportionally to dilution. As a result, the use of higher dilutions reduces our ability to remove spurious peaks caused by the pre-seeded ions via the simple subtraction approach.

The dilution-independence of the results for the monomodal mass spectra measured at low HABs is not surprising since the compounds composing the first mode are not expected to stem from self-collisions of the flame products in the dilution sampling system. On the other hand, one should clarify if the same independence can be observed for other modes that appear to be related to the "cluster modes" that line up in the mass defect plots.

Inspection of Fig. 6 reveals that the measured dilution-corrected number concentrations of the collision-charged flame products increase when using larger dilutions so that the detection of the third mode around 1200Th is enabled in negative polarity for the sample extracted at HAB = 10 mm with DR/Δt of ≈60 ms^{-1}.

Such a change is likely related to an increase in the value of the ionization efficiency that is not accounted for in the data analysis and is caused by the increase in the relative number concentration of the pre-seeded ions compared to that of the sampled and diluted flame materials (i.e., the same effect that causes the data to become progressively noisier at higher dilution). Indeed the relative number concentration of ions is known to control the ion-particle collision rate [50]. Additionally, excessive dilution can bring the number concentration of some modes below the detection limit of the APi-TOF, as observed for the results with DR/Δt of ≈212 ms^{-1} that are artificially deprived of the third mode in both polarities and also of the second mode in negative polarity at HAB = 7.5 mm (and only of the third mode in negative polarity at HAB = 10 mm).

Regardless of these minor data analysis complications caused by the unquantified efficiency of the collision charging method and its effect on the detection limit threshold, the results in Fig. 6 indicate that the conditions of dilution-independence have been achieved. Indeed, all the detected modes are retrieved at the same *m/z*, and along the same characteristic compositional lines, regardless of the dilution applied to the flame samples. Moreover, the number concentration of each mode relative to the other in the same mass spectra measured at the same HAB is also unaffected by the dilution level. This observation confirms the nontrivial fact that clustering of hydrocarbons with a molecular weight lighter than 400 Da and C/H between 2 and 3 originates in the flame at the same location where soot inception occurs. These clusters are prone to get preferentially a positive charge via collisions with either chem-ions in the flame [44] or with ions purposely pre-seeded in the dilution flow. Future studies are necessary to model quantitatively the collision charging mechanisms, infer an approximate value of the charging probability and reconcile the differences observed for measurements in opposite polarities.

4. Conclusions

An extremely gentle ion collision charging approach is implemented to perform APi-TOF high-resolution mass spectrometric analyses of materials with mass/charge up to 2000Th extracted through a rapid dilution probe from the incipiently sooting zone of a laminar premixed flame of ethylene and air. The approach consists of purposely pre-seeding ions in the dilution flow so that they can collide and charge/ionize the sampled flame products while they are transported from the sampling orifice to the mass spectrometer inlet. The simultaneous occurrence of dilution and charging of the analytes minimizes their transport time and, as a result, freezes any modification of their mass spectra due to self-collision growth (e.g., clustering/coagulation). Most importantly, the method allows one to analyze weakly bound molecular clusters that are initially neutral in the flame.

Other major findings are listed below.

1) Originally neutral flame products charged via collisions with the pre-seeded ions contain nitrogen and (mostly in negative polarity) oxygen in addition to hydrogen and carbon and are composed in approximately equal amounts of compounds with even (e.g., charged stable hydrocarbons) or odd (e.g., ionized radicals and/or protonated/deprotonated species [17,44]) values of the mass/charge, as opposed to the prevalently odd values of the mass/charge detected for materials naturally charged by the flame [44].
2) The detected flame generated materials that are charged in opposite polarities via collisions with the pre-seeded ions have a different elemental composition as evidenced by their mass defect plots and the products leading to soot inception are more prone to get a positive rather than a negative charge. Consequently, the results of measurements performed progressively further downstream in the flame, show a deoxygenation trend in negative polarity and the dehydrogenation trend typical of the transformations leading to soot inception for materials that get a positive charge.
3) Regardless of polarity and dilution, the detected flame materials quickly evolve from being monomodal (mass/charge smaller than 400Th) at HAB = 2.5 mm and 5 mm to multimodal (modal spacing of approximately 350–400Th) at HAB = 7.5 mm and 10 mm, where soot luminosity is present in the flame and results indicate that the observed clustering is intimately related to soot inception.
4) The polarity asymmetry in the overall elemental composition is progressively reduced at increasing HABs and almost vanishes at HAB = 7.5 mm and 10 mm, where the modes line up along a composition line of hydrocarbons with 2 < C/H < 3 in the mass defect plots, as a consequence of clustering of smaller compounds occurring at high temperature in the flame and/or at low temperature in the sampling tube. The trends observed for collision charged materials originally neutral in the flame are similar to those observed in previous a study for materials naturally charged by the flame [44].

5) The observed clustering leading to the identification of multiple modes in the mass spectra occurs at high-temperature in the flame and involves neutral compounds. This is the case because the elemental composition, relative number concentrations, and the mass/charge values of the modes are dilution-independent over the broad range of sample dilution conditions investigated in this study.

CRediT authorship contribution statement

Francesco Carbone: Conceptualization, Methodology, Validation, Investigation, Data curation, Writing - original draft, Writing - review & editing, Visualization, Project administration, Funding acquisition. **Manjula R. Canagaratna:** Software, Investigation, Resources, Writing - review & editing. **Andrew T. Lambe:** Software, Investigation, Resources, Writing - review & editing. **John T. Jayne:** Software, Resources, Project administration. **Douglas R. Worsnop:** Software, Resources, Project administration. **Alessandro Gomez:** Resources, Writing - review & editing, Project administration, Funding acquisition.

Declaration of Competing Interest

The authors declare that they have no known competing financial interests or personal relationships that could have appeared to influence the work reported in this paper.

Acknowledgments

F.C. gratefully acknowledges the financial support of the USA National Science Foundation (Grant #CBET- 2013382, Prof. Harsha K. Chelliah and Prof. John Daily serving as Program Managers) and, together with A.G., of Yale University. The authors are also thankful to Prof. Marshal Long of Yale University for lending the honeycomb burner.

References

[1] Janssen NA, Gerlofs-Nijland ME, Lanki T, Salonen RO, Cassee F, Hoek G, et al. Health effects of black carbon. 2012.
[2] Bond TC, Doherty SJ, Fahey DW, Forster PM, Berntsen T, Deangelo BJ, et al. Bounding the role of black carbon in the climate system: a scientific assessment. J Geophys Res Atmos 2013;118:5380–552. https://doi.org/10.1002/jgrd.50171.
[3] Bonne U, Homann KH, Wagner HGG. Carbon formation in premixed flames. Symp. Combust., vol. 10, Elsevier; 1965, p. 503–12. https://doi.org/10.1016/S0082-0784(65)80197-7.
[4] Haynes BS, Wagner HG. Soot formation. Prog Energy Combust Sci 1981;7:229–73. https://doi.org/10.1016/0360-1285(81)90001-0.
[5] Bittner JD, Howard JB. Composition profiles and reaction mechanisms in a near-sooting premixed benzene/oxygen/argon flame. Symp Combust 1981;18:1105–16. https://doi.org/10.1016/S0082-0784(81)80115-4.
[6] Frenklach M, Clary DW, Gardiner WC, Stein SE. Detailed kinetic modeling of soot formation in shock-tube pyrolysis of acetylene. Symp Combust 1985;20:887–901. https://doi.org/10.1016/S0082-0784(85)80578-6.
[7] Homann KH. Formation of large molecules, particulates and ions in premixed hydrocarbon flames; progress and unresolved questions. Symp Combust 1985;20(857):70. https://doi.org/10.1016/S0082-0784(85)80575-0.
[8] Frenklach M, Wang H. Detailed modeling of soot particle nucleation and growth. Symp Combust 1991;23:1559–66. https://doi.org/10.1016/S0082-0784(06)80426-1.
[9] Richter H, Howard JB. Formation of polycyclic aromatic hydrocarbons and their growth to soot-a review of chemical reaction pathways. Prog Energy Combust Sci 2000;26:565–608. https://doi.org/10.1016/S0360-1285(00)00009-5.
[10] D'Anna A, Violi A, D'Alessio A, Sarofim AF. A reaction pathway for nanoparticle formation in rich premixed flames. Combust Flame 2001;127:1995–2003. https://doi.org/10.1016/S0010-2180(01)00303-0.
[11] Bockhorn H, D'Anna A, Sarofim AF, Wang H. Combustion generated fine carbonaceous particles. 2007. https://doi.org/10.5445/KSP/1000013744.
[12] D'Anna A. Combustion-formed nanoparticles. Proc Combust Inst 2009;32(I):593–613. https://doi.org/10.1016/j.proci.2008.09.005.
[13] Wang H. Formation of nascent soot and other condensed-phase materials in flames. Proc Combust Inst 2011;33:41–67. https://doi.org/10.1016/j.proci.2010.09.009.
[14] Carbone F, Gleason K, Gomez A. Probing gas-to-particle transition in a moderately sooting atmospheric pressure ethylene/air laminar premixed flame. Part I: gas phase and soot ensemble characterization. Combust Flame 2017;181:315–28. https://doi.org/10.1016/j.combustflame.2017.01.029.
[15] Carbone F, Moslih S, Gomez A. Probing gas-to-particle transition in a moderately sooting atmospheric pressure ethylene/air laminar premixed flame. Part II: Molecular clusters and nascent soot particle size distributions. Combust Flame 2017;181:329–41. https://doi.org/10.1016/j.combustflame.2017.02.021.
[16] "International Sooting Flame (ISF) Workshop" - Proceedings of the 2018 Workshop: ISF-4. Trinity College Dublin, July 27-28, 2018, Dublin, Ireland. http://www.adelaide.edu.au/cet/isfworkshop/.
[17] Johansson KO, Head-Gordon MP, Schrader PE, Wilson KR, Michelsen HA. Resonance-stabilized hydrocarbon-radical chain reactions may explain soot inception and growth. Science (80-) 2018;361:997–1000. https://doi.org/10.1126/science.aat3417.
[18] Zhao L, Kaiser RI, Lu W, Xu B, Ahmed M, Morozov AN, et al. Molecular mass growth through ring expansion in polycyclic aromatic hydrocarbons via radical–radical reactions. Nat Commun 2019;10:1–7. https://doi.org/10.1038/s41467-019-11652-5.
[19] Wang Y, Chung SH. Soot formation in laminar counterflow flames. Prog Energy Combust Sci 2019;74:152–238. https://doi.org/10.1016/j.pecs.2019.05.003.
[20] Schulz F, Commodo M, Kaiser K, De Falco G, Minutolo P, Meyer G, et al. Insights into incipient soot formation by atomic force microscopy. Proc Combust Inst 2019;37:885–92. https://doi.org/10.1016/j.proci.2018.06.100.
[21] Jacobson RS, Korte AR, Vertes A, Miller JH. The molecular composition of soot. Angew Chemie - Int Ed 2020;59:4484–90. https://doi.org/10.1002/anie.201914115.
[22] Frenklach M, Mebel AM. On the mechanism of soot nucleation. Phys Chem Chem Phys 2020;22:5314–31. https://doi.org/10.1039/d0cp00116c.
[23] Faccinetto A, Irimiea C, Minutolo P, Commodo M, D'Anna A, Nuns N, et al. Evidence on the formation of dimers of polycyclic aromatic hydrocarbons in a laminar diffusion flame. Commun Chem 2020;3:1–8. https://doi.org/10.1038/s42004-020-00357-2.
[24] Gleason K, Carbone F, Plata D, Summer AJ, Drollette BD, Gomez A. Small aromatic hydrocarbons control incipient soot formation. Combust Flame 2021;223:398–406. https://doi.org/10.1016/j.combustflame.2020.08.029.
[25] Michelsen HA, Colket MB, Bengtsson P-E, D'Anna A, Desgroux P, Haynes BS, et al. A Review of Terminology Used to Describe Soot Formation and Evolution under Combustion and Pyrolytic Conditions. ACS Nano 2020:acsnano.0c06226. https://doi.org/10.1021/acsnano.0c06226.
[26] Biordi JC. Molecular beam mass spectrometry for studying the fundamental chemistry of flames. Prog Energy Combust Sci 1977;3:151–73. https://doi.org/10.1016/0360-1285(77)90002-8.
[27] Roth P, Hospital A. Mass growth and coagulation of soot particles in low pressure flames. Symp Combust 1992;24:981–9. https://doi.org/10.1016/S0082-0784(06)80116-5.
[28] Dobbins RA, Fletcher RA, Lu W. Laser microprobe analysis of soot precursor particles and carbonaceous soot. Combust Flame 1995;100:301–9. https://doi.org/10.1016/0010-2180(94)00047-V.
[29] Hansen N, Cool TA, Westmoreland PR, Kohse-Höinghaus K. Recent contributions of flame-sampling molecular-beam mass spectrometry to a fundamental understanding of combustion chemistry. Prog Energy Combust Sci 2009;35:168–91. https://doi.org/10.1016/j.pecs.2008.10.001.
[30] Qi F. Combustion chemistry probed by synchrotron VUV photoionization mass spectrometry. Proc Combust Inst 2013;34:33–63. https://doi.org/10.1016/j.proci.2012.09.002.
[31] Skeen SA, Michelsen HA, Wilson KR, Popolan DM, Violi A, Hansen N. Near-threshold photoionization mass spectra of combustion-generated high-molecular-weight soot precursors. J Aerosol Sci 2013;58:86–102. https://doi.org/10.1016/j.jaerosci.2012.12.008.
[32] Reilly PTA, Gieray RA, Whitten WB, Ramsey JM. Direct observation of the evolution of the soot carbonization process in an acetylene diffusion flame via real-time aerosol mass spectrometry. Combust Flame 2000;122:90–104. https://doi.org/10.1016/S0010-2180(00)00105-X.
[33] Grotheer HH, Pokorny H, Barth KL, Thierley M, Aigner M. Mass spectrometry up to 1 million mass units for the simultaneous detection of primary soot and of soot precursors (nanoparticles) in flames. Chemosphere 2004;57:1335–42. https://doi.org/10.1016/j.chemosphere.2004.08.054.
[34] Öktem B, Tolocka MP, Zhao B, Wang H, Johnston MV. Chemical species associated with the early stage of soot growth in a laminar premixed ethylene-oxygen-argon flame. Combust Flame 2005;142:364–73. https://doi.org/10.1016/j.combustflame.2005.03.016.
[35] Maricq MM. An examination of soot composition in premixed hydrocarbon flames via laser ablation particle mass spectrometry. J Aerosol Sci 2009;40:844–57. https://doi.org/10.1016/j.jaerosci.2009.07.001.
[36] Adamson BD, Skeen SA, Ahmed M, Hansen N. Detection of aliphatically bridged multi-core polycyclic aromatic hydrocarbons in sooting flames with atmospheric-sampling high-resolution tandem mass spectrometry. J Phys Chem A 2018;122:9338–49. https://doi.org/10.1021/acs.jpca.8b08947.
[37] Adamson BA, Skeen SA, Ahmed M, Hansen N. Nucleation of soot : experimental assessment of the role of polycyclic aromatic hydrocarbon (PAH) dimers. Z Phys Chemie 2020;234:1295–310. https://doi.org/10.1515/zpch-2020-1638.
[38] Apicella B, Carpentieri A, Alfè M, Barbella R, Tregrossi A, Pucci P, et al. Mass spectrometric analysis of large PAH in a fuel-rich ethylene flame. Proc Combust Inst 2007;31(I):547–53. https://doi.org/10.1016/j.proci.2006.08.014.
[39] Irimiea C, Faccinetto A, Mercier X, Ortega IK, Nuns N, Therssen E, et al. Unveiling trends in soot nucleation and growth: when secondary ion mass spectrometry meets statistical analysis. Carbon N Y 2019;144:815–30. https://doi.org/10.1016/j.carbon.2018.12.015.

[40] Zamith S, L'Hermite JM, Dontot L, Zheng L, Rapacioli M, Spiegelman F, et al. Threshold collision induced dissociation of pyrene cluster cations. J Chem Phys 2020;153:054311. https://doi.org/10.1063/5.0015385.
[41] Erickson HP. Size and shape of protein molecules at the nanometer level determined by sedimentation, gel filtration, and electron microscopy. Biol Proced Online 2009;11:32–51. https://doi.org/10.1007/s12575-009-9008-x.
[42] Prasad S, Mandal I, Singh S, Paul A, Mandal B, Venkatramani R, et al. Near UV-Visible electronic absorption originating from charged amino acids in a monomeric protein. Chem Sci 2017;8:5416–33. https://doi.org/10.1039/c7sc00880e.
[43] Carbone F, Attoui M, Gomez A. Challenges of measuring nascent soot in flames as evidenced by high-resolution differential mobility analysis. Aerosol Sci Technol 2016;50:740–57. https://doi.org/10.1080/02786826.2016.1179715.
[44] Carbone F, Canagaratna MR, Lambe AT, Jayne JT, Worsnop DR, Gomez A. Exploratory analysis of a sooting premixed flame via on-line high resolution (APi-TOF) mass spectrometry. Proc Combust Inst 2019;37:919–26. https://doi.org/10.1016/j.proci.2018.08.020.
[45] Zhao B, Yang Z, Wang J, Johnston MV, Wang H. Analysis of soot nanoparticles in a laminar premixed ethylene flame by scanning mobility particle sizer. Aerosol Sci Technol 2003;37:611–20. https://doi.org/10.1080/02786820300908.
[46] Maricq MM. Size and charge of soot particles in rich premixed ethylene flames. Combust Flame 2004;137:340–50. https://doi.org/10.1016/j.combustflame.2004.01.013.
[47] Junninen H, Ehn M, Petäjä T, Luosujärvi L, Kotiaho T, Kostiainen R, et al. A high-resolution mass spectrometer to measure atmospheric ion composition. Atmos Meas Tech 2010;3:1039–53. https://doi.org/10.5194/amt-3-1039-2010.
[48] Maißer A, Thomas JM, Larriba-Andaluz C, He S, Hogan CJ. The mass-mobility distributions of ions produced by a Po-210 source in air. J Aerosol Sci 2015;90:36–50. https://doi.org/10.1016/j.jaerosci.2015.08.004.
[49] Liu Y, Attoui M, Yang K, Chen J, Li Q, Wang L. Size-resolved chemical composition analysis of ions produced by a commercial soft X-ray aerosol neutralizer. J Aerosol Sci 2020;147:105586. https://doi.org/10.1016/j.jaerosci.2020.105586.
[50] Hoppel WA, Frick GM. The nonequilibrium character of the aerosol charge distributions produced by neutralizes. Aerosol Sci Technol 1990;12:471–96. https://doi.org/10.1080/02786829008959363.
[51] Hughey CA, Hendrickson CL, Rodgers RP, Marshall AG, Qian K. Kendrick mass defect spectrum: a compact visual analysis for ultrahigh-resolution broadband mass spectra. Anal Chem 2001;73:4676–81. https://doi.org/10.1021/ac010560w.
[52] Ude S, De La Mora JF. Molecular monodisperse mobility and mass standards from electrosprays of tetra-alkyl ammonium halides. J Aerosol Sci 2005;36:1224–37. https://doi.org/10.1016/j.jaerosci.2005.02.009.
[53] Moini M. Ultramark 1621 as a calibration/reference compound for mass spectrometry. II. Positive- and negative-ion electrospray ionization. Rapid Commun Mass Spectrom 1994;8:711–4. https://doi.org/10.1002/rcm.1290080910.
[54] Zhang X, Krechmer JE, Groessl M, Xu W, Graf S, Cubison M, et al. A novel framework for molecular characterization of atmospherically relevant organic compounds based on collision cross section and mass-to-charge ratio. Atmos Chem Phys 2016;16:12945–59. https://doi.org/10.5194/acp-16-12945-2016.
[55] Fuchs NA. On the stationary charge distribution on aerosol particles in a bipolar ionic atmosphere. Geofis Pura e Appl 1963;56:185–93. https://doi.org/10.1007/BF01993343.